

Coded wavefront sensing for video-rate quantitative phase imaging and tomography: validation with digital holographic microscopy

SYED MUHAMMAD KAZIM,^{1,*} FRANZISKA STRASSER,² MIA KVÅLE LØVMO,² ANDRII NEHRYCH,¹ SIMON MOSER,² MICHAŁ ZIEMCZONOK,³ WOLFGANG HEIDRICH,⁴ IVO IHRKE,¹ AND MONIKA RITSCH-MARTE²

¹Zentrum für Sensorsysteme, University of Siegen, Paul-Bonatz-Str. 9-11, 57076 Siegen, Germany

²Institute of Biomedical Physics, Medical University of Innsbruck, Müllerstr. 44, 6020 Innsbruck, Austria

³Warsaw University of Technology, Institute of Micromechanics and Photonics, św. Andrzeja Boboli 8, 02-525 Warsaw, Poland

⁴Visual Computing Center, King Abdullah University of Science and Technology, Building 1 (Al Khwarizmi) West, Level 2, Thuwal 23955-6900, Saudi Arabia

*syed.kazim@uni-siegen.de

Abstract: We demonstrate coded wavefront sensing (Coded WFS) for video-rate quantitative phase imaging and 3D refractive index (RI) tomography of biological specimens. To evaluate the accuracy, we implement an experimental setup that supports measurements of specimens with Coded WFS as well as with digital holographic microscopy (DHM) under identical conditions, enabling direct comparison. We image a static 3D phantom fabricated via additive manufacturing and a rotating HEK293 cell in an acoustofluidic chamber. Our results demonstrate good agreement between the two methods, with the advantage that, in contrast to DHM, Coded WFS enables simple integration with standard microscopes. Furthermore, we apply a standard tomographic reconstruction algorithm to the HEK293 cell data for comparison, which demonstrates the potential of Coded WFS in tomography.

1. Introduction

The volumetric distribution of the refractive index (RI) in cells is linked to biologically relevant structures in their interior [1]. RI tomography enables the recovery of volumetric RI distributions in inhomogeneous specimens such as biological cells, enabling a quantitative characterization of their morphology. It holds great potential for a non-invasive and quantitative study of intracellular matter as it utilizes the intrinsic phase contrast without the need for staining and genetic modifications to create fluorescent markers [2–4].

RI tomography is based on i) quantitative phase imaging (QPI) techniques that enable the label-free imaging of phase specimens and ii) a set of measurements under varying illumination and/or viewing conditions:

i) Digital holographic microscopy (DHM) [5–7] is the gold standard of QPI as it provides reliable, high-resolution access to the complex wavefields. QPI methods can be grouped into two categories: *Single-shot QPI-capable methods*, for example, those that record interferograms, such as DHM, and *computational methods* that record the intensity two or more times, usually at different focus planes, including transport of intensity-based methods [8–10], using optimization algorithms to recover the quantitative phase. The latter group is inherently challenging for snapshot QPI. Even though Coded WFS belongs to this category, the reference image can be taken offline and it is, therefore, snapshot-capable.

ii) The required actuation of the specimens can be achieved by mechanical confinement to a tip or in a capillary attached to a rotation stage [11]. Alternatively, contactless manipulation is a promising research avenue, that has, e.g., been achieved by using optical tweezers to rotate

46 suspended biological cells [12]. Optical trapping for the manipulation of arbitrarily shaped
47 specimens without prior geometric information has also been successfully demonstrated [13].
48 Acoustic forces have also been used to position and rotate a suspended specimen [14–16]. An
49 alternative method is to provide angled illumination to a static specimen [17, 18]. However, this
50 setup generally suffers from the missing cone problem as the range of angles is smaller. For
51 QPI-based tomography, retrieved complex wavefields from multiple viewing directions have
52 been combined to yield volumetric RI distribution [11–14, 17–20].

53 In this paper, we propose Coded WFS [21] as a promising candidate for QPI-based 3D
54 RI tomography due to its affordability, single-shot capability, and seamless integration with
55 standard microscopes. We integrate an acoustofluidic device [16] in our setup, enabling specimen
56 rotation and contactless measurements from a full 360° range of viewing angles. This setup fully
57 leverages the benefits of QPI while simultaneously reducing the hardware overhead associated
58 with interferometric methods. In the following, we review both DHM and Coded WFS, as well
59 as RI tomography.

60 **Holographic Microscopy.** DHM is an established interferometry-based snapshot QPI method,
61 which inherently offers support for video-rate phase imaging [22, 23]. Gabor originally introduced
62 holographic imaging in an attempt to improve the resolution in electron microscopy [24, 25]. The
63 field of digital holography was only later developed, distinguishing itself from holographic imaging
64 in that it recorded the hologram electronically and not on film [26]. DHM is the application of
65 digital holography to microscopic imaging and has found widespread application in this area due
66 to its ability to measure the phase contrast of objects with high precision [22, 23, 27, 28].

67 In off-axis DHM, the interference of the object wave with a tilted plane wave ensures that
68 the amplitude and phase of the specimen can be encapsulated within a single intensity image.
69 DHM retrieves the propagated phase of the specimen in the image plane, which is then digitally
70 propagated back to the object plane [5]. The retrieved quantitative phase measures the optical
71 path difference of the specimen along a single axis.

72 Digital holography remains an active research field for microscopy, tomography, cell identifi-
73 cation, and more, as is comprehensively explored in [29]. Moreover, the high accuracy of the
74 recovered phase maps has made DHM the default choice to not only benchmark the performance
75 of other QPI methods but also to evaluate the quality of fabrication processes of sub-micrometer
76 3D phantoms [30–32].

77 However, DHM requires careful setup and dedicated hardware for its realization, including
78 damped optical tables and lasers, which makes integration with other optical systems challenging.
79 For more extended 3-dimensional objects, undoing phase wrapping, which occurs when the optical
80 path difference (OPD) exceeds the illumination wavelength, requires additional consideration.

81 **Coded Wavefront Sensing.** Another class of QPI methods includes wavefront sensors
82 operating on the same principle as the Hartmann test, which treats the specimen wavefront as
83 transverse aberrations compared to an ideal wavefront [33]. The Hartmann sensor involves an
84 array of apertures a short distance away from the image plane and tracks the motion of diffraction
85 spots relative to their ideal positions due to a non-ideal wavefront and integrates the resulting
86 vector field to retrieve the phase of the specimen.

87 The aperture array is replaced with a lenslet array to improve the light efficiency in the
88 Shack-Hartmann wavefront sensor (SHWS) [34]. The size of the lenslets has also been reduced
89 to increase the spatial resolution of the SHWS [35]. However, as a consequence, the range of
90 movement for the diffraction spots that can be tracked unambiguously, corresponding to the
91 lenslet size, also reduces. Smaller regions restrict SHWSs to the measurement of small distortions.
92 SHWSs are, therefore, limited by a fundamental trade-off.

93 It is possible to replace the lenslet arrangement with a thin diffuser or a random phase
94 mask [36–39]. This changes the reference image from a regular grid of spots to a random speckle
95 pattern and enables continuous tracking of the resulting deformation of the speckle grains. We

96 refer to these QPI methods as coded wavefront sensing [39].

97 Coded WFS requires a reference-specimen pair of intensity images, where the reference is
98 measured only once for an optical setup. The reference speckle pattern is the diffraction pattern
99 of the phase mask, recorded in the absence of a specimen. A second speckle pattern is recorded
100 after inserting the specimen in the optical system. Coded WFS leverages a useful phenomenon
101 known as the optical memory effect [40–42], which relates local tips or tilts in the wavefront
102 incident on the phase mask with local shifts in the reference. In Coded WFS, the motion of
103 the pixels between the reference-specimen pair provides information about the gradient of the
104 phase of the specimen. Optical flow-inspired [43] methods are used to track the motion, which is
105 integrated to obtain the quantitative phase of the specimen.

106 More recently, algorithmic advancements in Coded WFS have allowed the simultaneous
107 recovery of amplitude and phase of weakly absorbing phase objects [21]. Like DHM, Coded
108 WFS is a snapshot method that allows QPI at video rates. However, Coded WFS is readily
109 integrable with bright-field microscopes, leading to less stringent hardware requirements and a
110 higher potential of being implemented in standard laboratories.

111 **Refractive Index Tomography.** Given several input phase maps under different known
112 incident illumination and/or observation directions, the 3D RI distribution of a specimen may be
113 determined in a process known as optical diffraction tomography first described by Wolf [44, 45].
114 It is based on the Fourier diffraction theorem (FDT) [46, 47] which states that, in the case of
115 weakly scattering objects, the Fourier transform of the field is related to a hemispherical surface
116 in the Fourier transform of scattering potential of the specimen. First practical demonstrations of
117 RI tomography on biological samples were implemented using DHM [11] and utilized optical
118 projection tomography which can be used in conditions where the scattering angles are sufficiently
119 small to enable the use of the Fourier slice theorem (FST) instead of the FDT [18, 19]. Joint
120 absorption and RI tomography based on mechanical scanning of the specimen has been described
121 earlier in [48]. Recent developments include combinations with structured illumination [3], and
122 deconvolution-based recovery from focal stacks [4]. Improved forward models can extend the
123 range of the scattering regime beyond the Born approximation [49–52].

124 **Overview.** In Sec. 2, we briefly review the QPI techniques DHM and Coded WFS, where
125 DHM is used as a gold standard to validate Coded WFS as a technique for snapshot QPI, as well
126 as the acoustofluidic trapping device which is fundamental for our dynamic QPI experiments that
127 serve as 3D RI tomography inputs. We provide the details of the experimental setup in Sect. 3.1,
128 which enables imaging the specimen in an identical setting by both methods. We validate the QPI
129 accuracies in Sect. 3.2 by imaging a phantom with a known design OPD: a 3D-printed cluster
130 of objects resembling HeLa cells. We then showcase their video capabilities in Sect. 3.3 by
131 performing video-rate QPI on a real rotating HEK293 cell, where the sustained and periodic
132 rotation of the cell in the acoustofluidic device enables a fair comparison. In Sect. 3.4, we
133 estimate the 3D RI distribution of the HEK cell. We provide a discussion and draw conclusions
134 in Sect. 4.

135 **2. Methods**

136 *2.1. Digital Holographic Microscopy*

137 In standard off-axis digital holography, coherent plane wave illumination is split into an object
138 beam that is modulated by the specimen and a reference beam that is tilted by a mirror. The wave
139 fields are combined and measured in the sensor plane. The interference of the object beam with
140 a tilted plane wave ensures that the spectrum of the measurement contains an easily separable
141 propagated transfer function of the unknown specimen, where the separation is governed by the
142 amount of reference beam tilt. Off-axis DHM has been comprehensively developed and analyzed
143 in [6, 7, 53, 54].

144 DHM offers dependable snapshot QPI capabilities, which has also been leveraged to benchmark
 145 the performance of newly developed methods [30, 31]. In this paper, we use a common-path
 146 shearing interferometer inspired by [6], tailored for use with the acoustofluidic device. Instead of
 147 using a pinhole to generate the reference wave, this DHM variant introduces a spatial shift on the
 148 (unfiltered) reference wave, such that a flat part of the beam is overlapped with the location of the
 149 object at an angle in the sensor plane. This necessitates that the sample is sparsely distributed,
 150 which is fulfilled in our case due to the nodes in the acoustic trapping potential. This precludes
 151 the need to consider path matching inside the microscope. The schematic of the setup is shown
 152 in Fig. 1 **a**.

153 2.2. Coded Wavefront Sensing

154 In Coded WFS, a random phase mask that modulates the phase of the incident wave is placed
 155 in close proximity (≈ 1 mm) to the camera sensor. In the absence of the specimen, plane wave
 156 illumination generates a speckle pattern in the image plane, which serves as the reference image,
 157 $I_0(r)$, for the setup. Subsequently, the unknown phase specimen, $e^{i\phi(r)}$, is inserted in the object
 158 plane of the optical setup. The modified speckle pattern in the image plane is measured and is
 159 referred to as the object image, $I(r)$.

160 The relation between $I_0(r)$ and $I(r)$ is estimated by leveraging the optical memory effect [40, 41],
 161 using the fact that the local changes in the speckle pattern, measured by the apparent flow of the
 162 pixels $u(r)$, are proportional to the gradient of the phase of the unknown specimen,

$$u(r) = \frac{z}{k} \nabla \phi(r), \quad (1)$$

163 where, z is the optical distance between the mask and the sensor determined in a calibration
 164 step [21], $k = \frac{2\pi}{\lambda_0}$ is the wavenumber and λ_0 is the illumination wavelength in vacuum.
 165 Consequently, the measurements can be written as,

$$I(r) = I_0(r - u(r)), \quad (2)$$

166 which simplifies wavefront sensing to an optical flow optimization problem [43] to estimate
 167 $u(r)$. Either $u(r)$ can be first estimated and then integrated to retrieve the OPD [38, 55], or an
 168 optimization strategy can be devised to estimate the OPD from $I(r)$ and I_0 in a single step as
 169 proposed in [39].

170 In this paper, we use the formulation in [21], which allows the unwrapped phase estimation of
 171 specimens with weak absorption while also providing the speckle-free bright-field amplitude
 172 of the specimen. Moreover, as Coded WFS has been shown to work well with broadband (or
 173 white-light) illumination [21, 38], we integrate a white-light illumination unit in the combined
 174 experimental setup in Sect. 3.1.

175 2.3. Acoustofluidic Trapping Device

176 To image trapped and rotating single cells, we employ an acoustofluidic platform developed
 177 in [16] shown in Fig. 1 **b**. The device is tailored for transmission imaging and mounted on an
 178 inverted light microscope. Bulk acoustic waves are generated by three lithium niobate (LiNbO_3)
 179 transducers coupled to a fluid-filled chamber to generate standing waves in three orthogonal
 180 directions. The sample is introduced via microfluidic channels into the middle of the chamber
 181 where all three acoustic waves intersect. The optically transparent vertical transducer levitates
 182 the sample and grants optical access for illumination. The channels are milled in an aluminum
 183 carrier and the bottom of the chamber is sealed with a cover slip acting as a reflector for the
 184 vertical sound waves and ensuring imaging compatibility. By tuning the relative amplitudes of
 185 the three acoustic waves we control the trapping in 3D and the sample orientation. To induce
 186 sustained rotations of the sample around an axis orthogonal to the imaging axis, we tune the

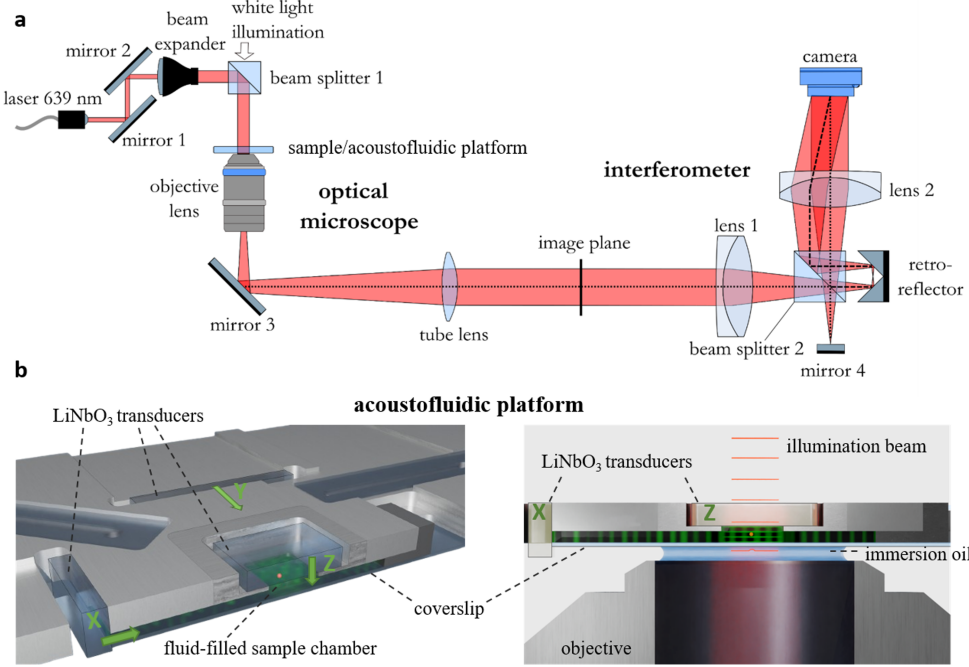


Fig. 1. **a** Experimental setup. The sample is mounted on a commercial inverted microscope (Nikon ECLIPSE Ti2-E) and separately illuminated by two sources: A fibre-coupled diode laser for DHM and a broadband LED for Coded WFS. The scattered light by the specimens is collected using a water immersion objective (1.15 NA, 40x), and two output ports of the microscope are operated sequentially for dynamic measurements. **b** Acoustofluidic platform. Schematics of the acoustofluidic platform with an angled top view and a cross-section. The propagation direction of the ultrasound from the three orthogonal LiNbO₃ transducers in x-, y- and z-direction are indicated with green arrows.

187 relative phase and amplitude of the vertical and one horizontal transducer driven at the same
 188 frequency (5th harmonic frequency around 20 MHz). The rotating sample maintains rotation
 189 periodicity, ensuring comparable successive revolutions. To record the specific background, the
 190 sample is acoustically moved out of the field of view by tuning the respective frequency.

191 3. Experiments and Results

192 3.1. Combined Experimental Setup

193 Our experimental platform is schematically shown in Fig. 1 **b**. The sample chambers and the
 194 acoustic device are mounted on a commercial inverted light microscope (Nikon ECLIPSE Ti2-E).
 195 The QPI measurement systems, DHM and Coded WFS, are installed on two separate observation
 196 ports, labeled image plane in Fig. 1 **a**.

197 In the DHM setting the sample is illuminated by a collimated beam from a fibre coupled
 198 diode laser (TOPTICA iBeam smart, $\lambda = 640$ nm). The light scattered by the sample is
 199 collected by an objective lens (Nikon CFI Apochromat LWD Lambda-S 40 \times NA 1.15, water
 200 immersion) and imaged onto either of the two output ports of the microscope. A home-built
 201 common path shearing interferometer based on [6] enables phase-stable DHM measurements
 202 with trans-illumination through the acoustofluidic device. We record off-axis interferograms on

203 a camera (mvBlueFOX3-2071) to obtain quantitative information about the amplitude and the
204 phase of the optical field.

205 In the Coded WFS case, we use a broadband white LED (Thorlabs MWWHL4) with a smooth
206 spectrum (color temperature 3000K) for illumination. It is mounted on the microscope after
207 tilting back the original illumination module. We used a lens to focus the LED illumination
208 onto the sample, increasing the illumination throughput. For the operation of the Coded WFS, it
209 is necessary to capture a single reference image. For static samples, we move the observation
210 region, and with the acoustofluidic chip, we acoustically move the sample out of the field of
211 view. Afterwards, we set the target observation region and capture images of static or moving
212 objects. The Coded WFS consists of a random binary phase mask, positioned 1.43 mm in front
213 of a monochromatic sensor (Thorlabs 1501M-USB-TE), replacing the protection cover glass [21].

214 In order to create phase videos, we mount the acoustofluidic trapping device on the microscope
215 stage to trap and rotate individual fixated HEK 293 cells.

216 *3.2. Validation Experiments*

217 To verify the QPI capabilities of our Coded WFS setup against the DHM, a 3D-printed cluster
218 of artificial ‘HeLa cells’ was imaged. The fabrication was performed using a two-photon
219 polymerization lithography system, which enables 3D printing of structures of variable height on
220 top of microscopy slides [32]. Identical models of HeLa cells, manufactured using a polymer
221 with a RI of 1.55 at 633 nm, are placed in different orientations to form a cluster, where the
222 maximum designed height of each cell is $\approx 8.4 \mu\text{m}$. The height map was converted to an OPD
223 map (in μm) by taking the product $h(r)\Delta\eta$, where h is the height and $\Delta\eta = 0.038$ is the RI
224 contrast, considering immersion of the model in Zeiss Immersol 518F (RI = 1.512 at 640 nm),
225 and is referred to as Phantom Design in Fig. 2 a.

226 The fabricated cluster is correspondingly immersed in Immersol 518F prior to imaging. Fig. 2 a
227 shows the retrieved phases of the phantom using DHM and Coded WFS. Figs. 2 b and c compare
228 the cross-sections and the pixel-wise absolute differences, respectively, of the OPDs retrieved
229 by the two techniques with the designed OPD map of the phantom. The results, in addition to
230 validating Coded WFS, demonstrate that non-planar reference waves can be used for Coded WFS
231 in this setting, providing advantages in system setup.

232 The minor disagreements between the measured and designed OPDs are explained partially by
233 the limited accuracy of the fabrication process. Fabrication of variable-height structures using
234 this method has been found to deviate from the ideal design maps due to anisotropic shrinkage
235 and varying energy dose of the polymerization beam. The discrepancies can occur due to the
236 shape of the structures and their positions within the printed field of view [32]. Therefore, we also
237 expect variation in the OPD profiles of different cells in the phantom. Nonetheless, printed 3D
238 phantoms replicating complex cells enable the quantitative comparison of different QPI systems
239 and serve as an intermediary step before imaging real dynamic cells.

240 To improve the quality of the acquired OPDs, the following additional steps were taken. In
241 DHM, we evaluate the complex field of the background (in the absence of the specimen), which
242 is subtracted from the complex field of the object, ensuring the removal of tilts and artifacts in
243 the background. For Coded WFS, the background is removed using a fit on the empty area of the
244 phase map. To evaluate phase delay relative to the background (immersion), the average phase
245 delay due to the immersion is subtracted.

246 *3.3. Quantitative Phase and Amplitude Imaging of Rotating Cells*

247 An inherent advantage of both DHM and Coded WFS over standard TIE-based curvature sensing
248 techniques [9] and other computational microscopy methods is that only a single image of the
249 specimen is required to recover the complex field at the image plane. For Coded WFS, the
250 reference image without the specimen is required only once for a specific optical setup, which

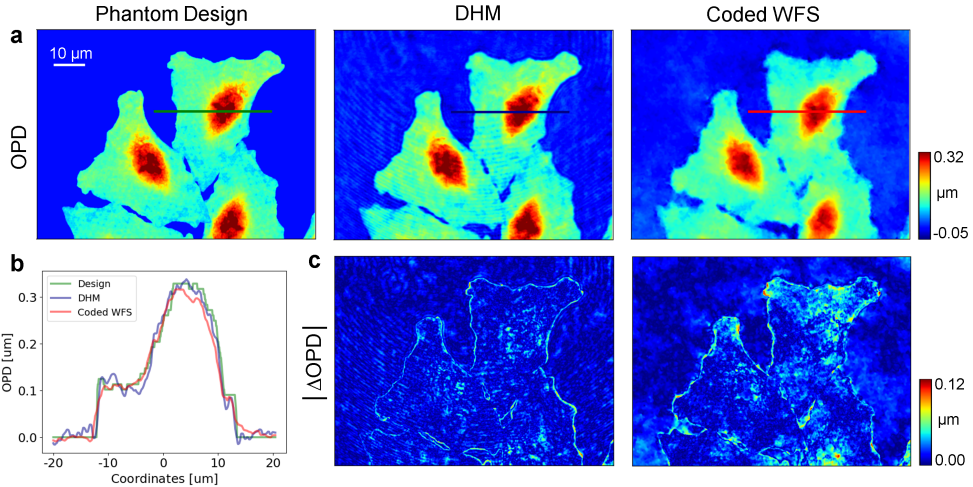


Fig. 2. Performance validation using 3D-printed cluster of artificial HeLa cells.

a Designed OPD map of the HeLa cell cluster and measured OPD maps of the fabricated phantom using DHM and Coded-WFS. **b** Cross-sections of the OPDs in **a** relative to the immersion. **c** The pixel-wise absolute difference $|\Delta\text{OPD}|$ between the designed OPD map and the OPDs retrieved using DHM (left) and Coded-WFS (right).

251 therefore does not hinder snapshot wavefront reconstruction.

252 We leverage the snapshot capabilities of DHM and Coded WFS to recover both the amplitudes
 253 and phases of cells at video rates ≈ 30 fps. A single HEK cell is trapped and actuated using
 254 the acoustofluidic trapping device described in Sect. 2.3 such that the cell rotates about an
 255 axis orthogonal to the imaging axis at $\approx 0.39 \text{ rad s}^{-1}$. The exposure times for DHM and
 256 Coded WFS are 1.5 ms and 2 ms, respectively. The combined experimental setup, described
 257 in Sect. 3.1, enables video recording of the rotating cell in identical conditions for DHM and
 258 Coded WFS as it leaves the microscope, including the acoustofluidic chamber in the specimen
 259 plane, entirely unchanged except for the illumination unit. A two-observation port microscope
 260 allows for designated installation points for DHM and Coded WFS, and common-path shearing
 261 interferometry precludes changes within the microscope, ensuring separation of the two QPI
 262 systems. The same HEK cell rotating with the same periodicity [16] is therefore recorded
 263 successfully by each system in succession.

264 Fig. 3 shows agreement between the retrieved intensities and phases of selected frames of
 265 the cell at different angles of rotation using DHM and Coded WFS. Coded WFS retrieves clear
 266 brightfield intensity images while DHM suffers from diffraction artifacts. However, the spatial
 267 resolution of the DHM reconstructions is observed to be qualitatively better than Coded WFS.
 268 The differences are more perceptible in the video (see **Visualization 1**), where a side-by-side
 269 comparison of intensities and phases retrieved by both methods for one complete rotation (485
 270 frames) is provided. Note that in both methods, the measurement rate is only limited by the
 271 camera hardware and not by the methods themselves. Therefore, due to the high temporal
 272 resolution of both DHM and Coded WFS, they are highly suitable to study dynamic specimens.

273 3.4. 3D Refractive Index Estimation

274 Traditional tomography setups use motorized mirror mounts to illuminate the specimen from
 275 different angles [18]. The finite angular extent of illumination leads to the missing cone problem,
 276 resulting in undesirable artifacts in the reconstruction. An alternative is to rotate the object by

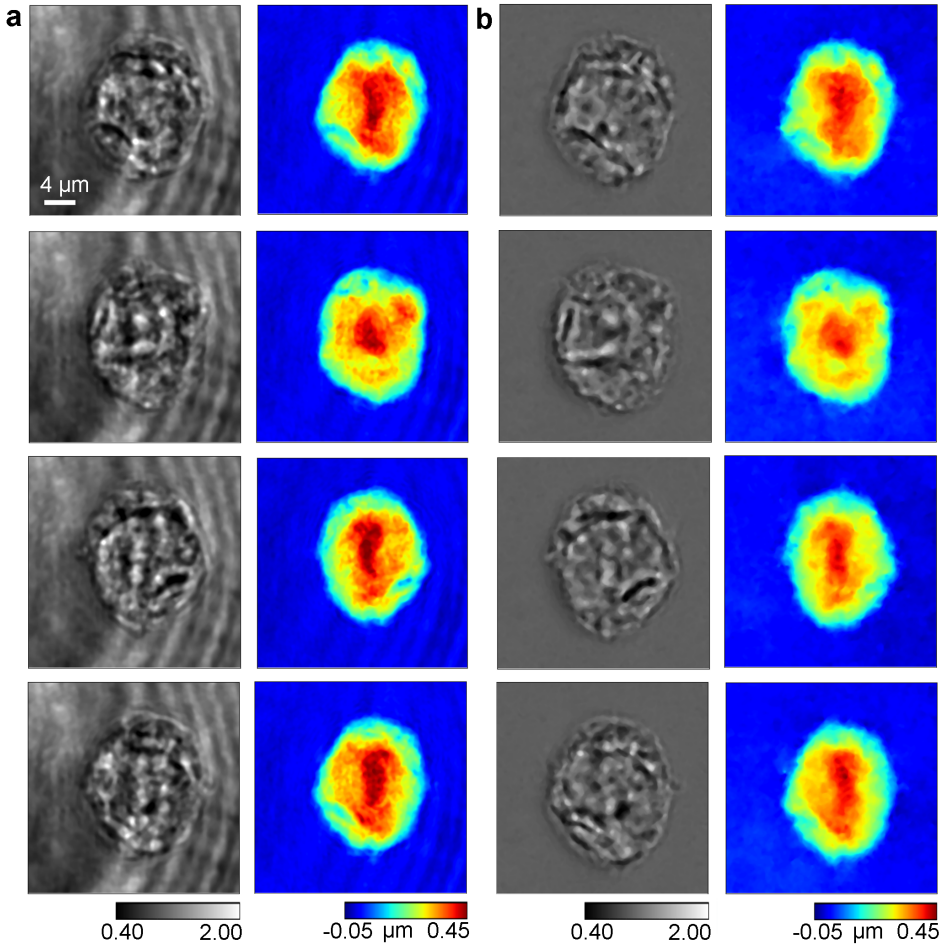


Fig. 3. Video-rate (≈ 30 fps) QPI. Quantitative reconstructions of intensity (left) and OPD (right) of corresponding frames using **a** DHM and **b** Coded WFS of a rotating HEK293 cell. The frames are chosen to reveal informative internal structures of the biological cell. Refer to the video (see **Visualization 1**) for one complete revolution of retrieved DHM and Coded WFS intensities and phases.

277 mechanical confinement and a motorized stage [11].

278 In comparison, the trapping and rotation of unknown objects using the acoustofluidic chamber
279 is both contactless and allows unimpeded access to 360° of viewing angles about one (or more)
280 object axis. However, because the object rotation is variable and unknown *a priori*, achieving an
281 accurate tomographic reconstruction becomes more involved [20, 56].

282 In this work, our goal is to showcase the simplicity of the hardware setup required for
283 tomography with a Coded WFS scheme and to verify the estimated RI distribution by comparing
284 it with DHM. For this purpose, we (i) retrieve the OPDs of the rotating HEK293 cell in Sect. 3.3
285 frame-by-frame, (ii) treat each OPD as a projection of the 3D RI distribution corresponding to a
286 pose (angle of rotation corresponding to a reference), and (iii) make the following approximations
287 for simplicity: First, since the precise pose information is not known, we approximate that
288 the poses are distributed uniformly. Second, we apply a low-pass spatial filter to (a) mitigate

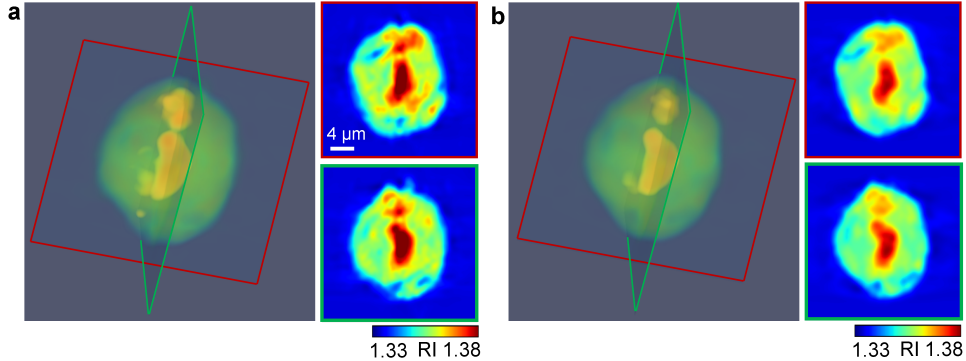


Fig. 4. 3D RI estimation. 3D RI distribution (left) and two slices (right) corresponding to the planes in the 3D visualization of a HEK293 cell estimated using 360°-view OPDs retrieved by **a** DHM and **b** Coded WFS.

289 specimen jitter and reduce perturbations between adjacent frames and (b) limit the frequency
 290 coverage of the data, enabling the use of the Fourier slice theorem (FST) for tomography.

291 We use the parallel geometry setting in the TIGRE toolbox [57] to simulate orthographic
 292 projection and the classical FDK algorithm [58] to estimate the 3D RI distribution of the HEK293
 293 cell, which is shown in the left of Figs. 4 **a** and **b**. To inspect the quantitative RI, we examine two
 294 slices corresponding to the planes highlighted in the 3D visualization, where each point on the
 295 plane is an RI. **Visualization 2** showcases the 360° view of the 3D RI distribution retrieved by the
 296 two methods. Even though no ground truth is available, the recovered RI range is in agreement
 297 with expected values [1].

298 While the approximations enable quick and easy 3D RI estimation, they reduce the fidelity of
 299 the tomographic reconstruction. Analyzing the spectrum of the OPD projections reveals that
 300 most of the energy is concentrated in the region where the Fourier diffraction theorem (FDT)
 301 arcs are approximately linear (see Supplement 1, Section 1 for details). This allows us to apply
 302 FST, provided we filter out the remaining spectrum. However, this approach comes at the cost
 303 of losing the ability to retrieve high-frequency structures. Moreover, the pose approximation is
 304 only accurate for objects with a spherical cross-section and a homogeneous density distribution.
 305 Considering a large frequency support without optimizing the poses first may introduce artifacts
 306 into the reconstruction.

307 4. Discussion and Conclusion

308 We have proposed and validated a novel approach to 3D RI tomography for individual cells: the
 309 acoustofluidic manipulation of the cell to enable the acquisition of 360 degree object poses in
 310 combination with video-rate QPI implemented via Coded WFS. Our approach lends itself to an
 311 implementation in an unmodified commercial microscope and, therefore has the potential to be
 312 widely applicable.

313 For validation, we have developed a combined experimental setup which enabled QPI using
 314 DHM and Coded WFS of phase specimens under identical experimental conditions. We have
 315 designed and fabricated a phantom replicating a cluster of cells, which enabled validation of
 316 phase accuracy of the Coded WFS method directly with the DHM.

317 The integration of the acoustofluidic chamber in the same setup allows for the levitation and
 318 rotation of biological cells. The retrieved intensities and phases of video-rate (≈ 30 fps) data,
 319 recorded sequentially for DHM and Coded-WFS, demonstrate good agreement, validating Coded

320 WFS as a suitable video-rate QPI method for our proposed technique. While DHM has been
321 previously applied to 3D RI tomography [11], this is the first time, to our knowledge, that Coded
322 WFS has been tested in this setting.

323 Our reported results rely on several restrictions and simplifying assumptions, namely i) a
324 weak scattering regime, ii) a roughly spherical shape of the specimen to assume a uniform
325 rotation over time, and iii) a limited maximum scattering angle caused by the specimen. Future
326 work will address these challenges and allow for higher 3D spatial resolutions. To address i),
327 multi-slice techniques in the forward model as e.g. in [52] would allow for stronger scattering to
328 be successfully treated. A more complex specimen shape will cause more irregular rotations since
329 the relevant forces apply varying amounts of torque at different object points. Pose estimation
330 of the specimen may solve this problem and address issue ii). Finally, improved reconstruction
331 algorithms can more fully account for the optical diffraction tomography geometry in the Fourier
332 domain, contributing to improve issue iii).

333 Summarizing, we believe that our proposed approach carries significant potential for a
334 simplified 3D RI tomography approach that may be well suited for a wide application.

335 **Funding.** This work was funded in part by the Austrian Science Fund (FWF) SFB 10.55776/F68
336 *Tomography Across the Scales*, project F6806-N36 Inverse Problems in Imaging of Trapped Particles and the
337 German Research Foundation under DFG FOR 5336 *Learning to Sense* project IH 114/2-1. For open access
338 purposes, the authors have applied a CC BY public copyright license to any author-accepted manuscript
339 version arising from this submission.

340 **Acknowledgement.** Monika Ritsch-Marte and Ivo Ihrke would like to thank the Institute for Pure and
341 Applied Mathematics (IPAM) at UCLA, where their current collaboration was initiated during the long
342 program "Computational Microscopy". We thank Judith Hagenbuchner and Michael Auerlechner (Medical
343 University Innsbruck) for providing us with the fixated HEK 293 cells. We thank Armin Sailer (Institute for
344 Experimental Physics, University of Innsbruck) for CNC-manufacturing the high-NA chip according to our
345 design.

346 **Disclosures.** The authors declare no conflicts of interest.

347 **Data availability.** Data underlying the results presented in this paper are not publicly available at this time
348 but may be obtained from the authors upon reasonable request.

349 **Supplemental document.** See Supplement 1 for supporting content.

350 **References**

- 351 1. P. Y. Liu, L. K. Chin, W. Ser, *et al.*, "Cell refractive index for cell biology and disease diagnosis: Past, present and
352 future," *Lab on a Chip* **16**, 634–644 (2016).
- 353 2. M. Habaza, M. Kirschbaum, C. Guernth-Marschner, *et al.*, "Rapid 3D refractive-index imaging of live cells in
354 suspension without labeling using dielectrophoretic cell rotation," *Adv. Sci.* **4**, 1600205 (2017).
- 355 3. S. Chowdhury, W. J. Eldridge, A. Wax, and J. Izatt, "Refractive index tomography with structured illumination,"
356 *Optica* **4**, 537–545 (2017).
- 357 4. H. Hugonnet, H. Hugonnet, M. Lee, *et al.*, "Optimizing illumination in three-dimensional deconvolution microscopy
358 for accurate refractive index tomography," *Opt. Express* **29**, 6293–6301 (2021).
- 359 5. E. Cuche, P. Marquet, and C. Depeursinge, "Spatial filtering for zero-order and twin-image elimination in digital
360 off-axis holography," *Appl. Opt.* **39**, 4070–4075 (2000).
- 361 6. P. Girshovitz and N. T. Shaked, "Compact and portable low-coherence interferometer with off-axis geometry for
362 quantitative phase microscopy and nanoscopy," *Opt. Express* **21**, 5701–5714 (2013).
- 363 7. E. Sánchez-Ortiga, A. Doblas, G. Saavedra, *et al.*, "Off-axis digital holographic microscopy: practical design
364 parameters for operating at diffraction limit," *Appl. Opt.* **53**, 2058–2066 (2014).
- 365 8. M. R. Teague, "Deterministic Phase Retrieval: A Green's Function Solution," *J. Opt. Soc. Am.* **73**, 1434–1441
366 (1983).
- 367 9. C. Zuo, J. Li, J. Sun, *et al.*, "Transport of Intensity Equation: a Tutorial," *Opt. Lasers Eng.* **135**, 106187 (2020).
- 368 10. P. F. Almoro, G. Pedrini, P. N. Gundu, *et al.*, "Phase microscopy of technical and biological samples through random
369 phase modulation with a diffuser," *Opt. Lett.* **35**, 1028–1030 (2010).
- 370 11. F. Charrière, A. Marian, F. Montfort, *et al.*, "Cell refractive index tomography by digital holographic microscopy,"
371 *Opt. Lett.* **31**, 178 (2006).

- 372 12. M. Habaza, B. Gilboa, Y. Roichman, and N. T. Shaked, “Tomographic phase microscopy with 180 rotation of live
373 cells in suspension by holographic optical tweezers,” *Opt. Lett.* **40**, 1881–1884 (2015).
- 374 13. K. Kim and Y. Park, “Tomographic active optical trapping of arbitrarily shaped objects by exploiting 3D refractive
375 index maps,” *Nat. Commun.* **8**, 15340 (2017).
- 376 14. T. Cacace, P. Memmolo, M. M. Villone, *et al.*, “Assembling and rotating erythrocyte aggregates by acoustofluidic
377 pressure enabling full phase-contrast tomography,” *Lab on a Chip* **19**, 3123–3132 (2019).
- 378 15. M. K. Løvmo, B. Pressl, G. Thalhammer, and M. Ritsch-Marte, “Controlled orientation and sustained rotation of
379 biological samples in a sono-optical microfluidic device,” *Lab on a Chip* **21**, 1563–1578 (2021).
- 380 16. M. K. Løvmo, S. Moser, G. Thalhammer-Thurner, and M. Ritsch-Marte, “Acoustofluidic trapping device for high-na
381 multi-angle imaging,” *Front. Phys.* **10**, 940115 (2022).
- 382 17. W. Choi, C. Fang-Yen, K. Badizadegan, *et al.*, “Tomographic phase microscopy,” *Nat. Methods* **4**, 717–719 (2007).
- 383 18. Y. Sung, W. Choi, C. Fang-Yen, *et al.*, “Optical diffraction tomography for high resolution live cell imaging,” *Opt.*
384 *Express* **17**, 266–277 (2009).
- 385 19. X. Ma, W. Xiao, and F. Pan, “Optical tomographic reconstruction based on multi-slice wave propagation method,”
386 *Opt. Express* **25**, 22595–22607 (2017).
- 387 20. S. Moser, M. Kvåle løvmo, F. Strasser, *et al.*, “Optical tomography reconstructing 3d motion and structure of
388 multiple-scattering samples under rotational actuation,” *bioRxiv* pp. 2024–11 (2024).
- 389 21. C. Wang, Q. Fu, X. Dun, and W. Heidrich, “Quantitative phase and intensity microscopy using snapshot white light
390 wavefront sensing,” *Sci. Reports* **9**, 13795 (2019).
- 391 22. E. Cuche, P. Marquet, and C. Depeursinge, “Simultaneous amplitude-contrast and quantitative phase-contrast
392 microscopy by numerical reconstruction of fresnel off-axis holograms,” *Appl. Opt.* **38**, 6994–7001 (1999).
- 393 23. P. Marquet, B. Rappaz, P. J. Magistretti, *et al.*, “Digital holographic microscopy: a noninvasive contrast imaging
394 technique allowing quantitative visualization of living cells with subwavelength axial accuracy,” *Opt. Lett.* **30**,
395 468–470 (2005).
- 396 24. D. Gabor, “A new microscopic principle,” *Nature* **161**, 777–778 (1948).
- 397 25. D. Gabor, “Microscopy by reconstructed wave-fronts,” *Proc. Royal Soc. London. Ser. A. Math. Phys. Sci.* **197**,
398 454–487 (1949).
- 399 26. J. Goodman and R. Lawrence, “Digital image formation from electronically detected holograms,” *Appl. Phys. Lett.*
400 **11**, 77–79 (1967).
- 401 27. T. Zhang and I. Yamaguchi, “Three-dimensional microscopy with phase-shifting digital holography,” *Opt. Lett.* **23**,
402 1221–1223 (1998).
- 403 28. K. M. Eder, A. Marzi, Á. Barroso, *et al.*, “Label-free digital holographic microscopy for in vitro cytotoxic effect
404 quantification of organic nanoparticles,” *Cells* **11**, 644 (2022).
- 405 29. B. Javidi, A. Carnicer, A. Anand, *et al.*, “Roadmap on digital holography,” *Opt. Express* **29**, 35078–35118 (2021).
- 406 30. J. M. Wittkopp, T. C. Khoo, S. Carney, *et al.*, “Comparative phase imaging of live cells by digital holographic
407 microscopy and transport of intensity equation methods,” *Opt. Express* **28**, 6123–6133 (2020).
- 408 31. S. Obando-Vásquez, M. J. Lopera, R. Restrepo, and C. Trujillo, “Comparative analysis of digital holographic
409 microscopy and digital lensless holographic microscopy for quantitative phase imaging,” *Opt. Continuum* **3**, 309–323
410 (2024).
- 411 32. S. Desissaire, M. Ziemczonok, T. Cantat-Moltrecht, *et al.*, “Bio-inspired 3d-printed phantom: Encoding cellular
412 heterogeneity for characterization of quantitative phase imaging,” *Measurement* **247**, 116765 (2025).
- 413 33. D. Malacara-Hernández and D. Malacara-Doblando, “What is a Hartmann test?” *Appl. Opt.* **54**, 2296–2301 (2015).
- 414 34. R. V. Shack and B. C. Platt, “Production and use of a lenticular Hartmann screen.” *J. Opt. Soc. Am. A* **61**, 656 (1971).
- 415 35. L. K. Saddlemeyer, G. Herriot, J.-P. Veran, and J. M. Fletcher, “Design aspects of the reconstructor for the Gemini
416 adaptive optics system (Altair),” in *Adaptive Optical System Technologies*, vol. 3353 (SPIE, 1998), pp. 150–159.
- 417 36. W. Harm, C. Roider, A. Jesacher, *et al.*, “Lensless imaging through thin diffusive media,” *Opt. Express* **22**,
418 22146–22156 (2014).
- 419 37. S. Bernet, W. Harm, A. Jesacher, and M. Ritsch-Marte, “Lensless digital holography with diffuse illumination
420 through a pseudo-random phase mask,” *Opt. Express* **19**, 25113–25124 (2011).
- 421 38. P. Berto, H. Rigneault, and M. Guillon, “Wavefront sensing with a thin diffuser,” *Opt. Lett.* **42**, 5117–5120 (2017).
- 422 39. C. Wang, X. Dun, Q. Fu, and W. Heidrich, “Ultra-high resolution coded wavefront sensor,” *Opt. Express* **25**,
423 13736–13746 (2017).
- 424 40. S. Feng, C. Kane, P. A. Lee, and A. D. Stone, “Correlations and fluctuations of coherent wave transmission through
425 disordered media,” *Phys. Rev. Lett.* **61**, 834–837 (1988).
- 426 41. I. Freund, M. Rosenbluh, and S. Feng, “Memory effects in propagation of optical waves through disordered media,”
427 *Phys. Rev. Lett.* **61**, 2328–2331 (1988).
- 428 42. H. Penketh and J. Bertolotti, “Imaging through scattering media by exploiting the optical memory effect: a tutorial,”
429 *J. Physics: Photonics* (2024).
- 430 43. B. K. Horn and B. G. Schunck, “Determining optical flow,” *Artif. Intell.* **17**, 185–203 (1981).
- 431 44. E. Wolf, “Three-dimensional structure determination of semi-transparent objects from holographic data,” *Opt.*
432 *Commun.* **1**, 153–156 (1969).
- 433 45. R. Dändliker and K. Weiss, “Reconstruction of the three-dimensional refractive index from scattered waves,” *Opt.*
434 *Commun.* **1**, 323–328 (1970).

- 435 46. A. C. Kak and M. Slaney, *Principles of Computerized Tomographic Imaging* (SIAM, 2001).
- 436 47. P. Müller, M. Schürmann, and J. Guck, “The theory of diffraction tomography,” (2016).
- 437 48. A. Barty, K. Nugent, A. Roberts, and D. Paganin, “Quantitative phase tomography,” Opt. Commun. **175**, 329–336
438 (2000).
- 439 49. U. S. Kamilov, I. N. Papadopoulos, M. H. Shoreh, *et al.*, “Learning approach to optical tomography,” Optica **2**, 517
440 (2015).
- 441 50. J. Lim, A. B. Ayoub, E. E. Antoine, and D. Psaltis, “High-fidelity optical diffraction tomography of multiple scattering
442 samples,” Light. Sci. & Appl. **8** (2019).
- 443 51. M. Chen, D. Ren, H.-Y. Liu, *et al.*, “Multi-layer born multiple-scattering model for 3d phase microscopy,” Optica **7**,
444 394 (2020).
- 445 52. S. Moser, A. Jesacher, and M. Ritsch-Marte, “Efficient and accurate intensity diffraction tomography of multiple-
446 scattering samples,” Opt. Express **31**, 18274–18289 (2023).
- 447 53. J. W. Goodman, *Introduction to Fourier optics* (Roberts and Company publishers, 2005).
- 448 54. J. Bühl, H. Babovsky, A. Kiessling, and R. Kowarschik, “Digital synthesis of multiple off-axis holograms with
449 overlapping fourier spectra,” Opt. Commun. **283**, 3631–3638 (2010).
- 450 55. L. Huang, M. Idir, C. Zuo, *et al.*, “Comparison of two-dimensional integration methods for shape reconstruction
451 from gradient data,” Opt. Lasers Eng. **64**, 1–11 (2015).
- 452 56. M. Kvåle Løvmo, S. Deng, S. Moser, *et al.*, “Ultrasound-induced reorientation for multi-angle optical coherence
453 tomography,” Nat. Commun. **15**, 2391 (2024).
- 454 57. A. Biguri, M. Dosanjh, S. Hancock, and M. Soleimani, “TIGRE: a MATLAB-GPU toolbox for CBCT image
455 reconstruction,” Biomed. Phys. & Eng. Express **2**, 055010 (2016).
- 456 58. L. A. Feldkamp, L. C. Davis, and J. W. Kress, “Practical cone-beam algorithm,” J. Opt. Soc. Am. A **1**, 612–619
457 (1984).